Lawrence Berkeley National Laboratory

Title

High performance metal-supported solid oxide fuel cells with infiltrated electrodes

Permalink

https://escholarship.org/uc/item/5hj0n3wk

Authors

Dogdibegovic, Emir
Wang, Ruofan
Lau, Grace Y
et al.

Publication Date

2019

DOI

10.1016/j.jpowsour.2018.11.004

Peer reviewed

High Performance Metal-Supported Solid Oxide Fuel Cells with Infiltrated Electrodes

Emir Dogdibegovic*, Ruofan Wang, Grace Y. Lau, and M.C. Tucker*

Lawrence Berkeley National Laboratory, Energy Storage and Distributed Resources Division,

1 Cyclotron Rd., MS 62-203, Berkeley, CA 94720, United States

*Corresponding authors:

Emir Dogdibegovic, Edogdibegovic@lbl.gov, Tel 1 (510)486-5635, Mail stop 62-R0313, 1

Cyclotron Road, Berkeley, CA 94720, United States

Michael C. Tucker, MCTucker@lbl.gov, Tel +1 (510)486-5304, Mail stop 62-R0203, 1

Cyclotron Road, Berkeley, CA 94720, United States

Abstract

High power density is required to commercialize solid oxide fuel cells for vehicular applications. In this work, high performance of metal supported solid oxide fuel cells (MS-SOFCs) is achieved via catalyst composition, electrode structure, and processing optimization. The full cell configuration consists of a dense ceramic electrolyte and porous ceramic backbones (electrodes) sandwiched between porous stainless steel metal supports. The conventional YSZ electrolyte and backbones are replaced with more conductive and thinner 10Sc1CeSZ ceramics. MS-SOFCs are co-sintered in a single step and subsequently infiltrated with nanocatalysts. Five categories of cathode catalysts are screened in full cells, including: perovskites, nickelates, praseodymium oxide, binary layered composites, and ternary layered composites. Various anode compositions are also tested. The conventional LSM cathode catalyst is replaced with more active Pr_6O_{11} and the Ni content of the SDC-Ni anode is increased. The resulting cells achieve a peak power of 1.56, 2.0, and 2.85 W cm^{-2} at 700, 750, and 800 °C, respectively, with 3%H_2O/H_2 as fuel and

cathode exposed to air. Multiple cells show reproducible performance (P_{max}=1.50 ± 0.06 W cm^{-2}) and OCV (1.10 ± 0.02 V). The performance is further increased with cathode exposed to pure oxygen (2.0 W cm^{-2} at 700 °C).

Keywords: Solid oxide fuel cell; Metal-support; Infiltration

1. Introduction

Metal-supported solid oxide fuel cells (MS-SOFCs) provide a number of advantages over conventional all-ceramic SOFCs. The symmetric-architecture MS-SOFC design developed at LBNL [1-3] includes thin ceramic backbones and electrolyte layer sandwiched between low-cost stainless steel supports. The LBNL design provides mechanical ruggedness, excellent tolerance to thermal [4] and redox cycling (critical in cases of disruption, intermittent fuel supply [5], or thermal fluctuations following load changes) [6], and extremely fast start-up capability [2, 7-11]. Furthermore, inexpensive FeCr-based ferritic stainless steel can significantly reduce the materials cost, and only a single co-sintering step is required, leading to lower fabrication cost. Infiltrating catalysts after cosintering ensures high performance, enabling vehicular applications [12]. Small passenger vehicles require high power due to limited volume to house the SOFC stack, and to provide immediate response during rapid vehicular acceleration and transient driving conditions, such as intermittent fuel flow and continuous load variation.

Introducing ferritic stainless steel to the cell materials set brings multiple challenges that must be addressed before successful deployment of MS-SOFCs. Above all, co-processing of the metal support and electro-catalysts is particularly challenging. All-ceramic SOFCs are sintered in air at elevated temperatures, but due to the presence of stainless steel, MS-SOFCs require sintering in reducing atmosphere to prevent metal oxidation. Reducing conditions are challenging for catalyst

processing. Nickel coarsening, cathode decomposition, and elemental inter-diffusion between the catalysts and the porous backbones may occur. Therefore, the symmetric structure MS-SOFC is cosintered in reducing conditions without catalysts. The resulting porous nature of the metal support and backbone allows for catalyst infiltration in air, which is the approach taken in this work. Through extensive efforts to achieve compatibility of the metal and YSZ backbone structure [12, 13], successful, singe step, co-sintering of MS-SOFCs in reducing environment was demonstrated at LBNL [2, 7, 12]. Matching thermal expansion, good bonding and chemical compatibility between the cell components, and low oxidation rates, suitable for the long lifetimes in stationary and mobile SOFC power plants have been demonstrated.[2, 7, 12]

It is desirable to operate MS-SOFCs in the temperature range of 650-700 °C, where there is a suitable tradeoff between performance and longevity. Higher operating temperature may lead to: (1) oxidation of the metal support ($\geq$800 °C) [2, 3], (2) accelerated Cr poisoning of the cathode catalyst [2, 14-17], and (3) rapid catalyst coarsening. However, lower operating temperature constrains the power density, which is the critical for commercialization of this technology in vehicles. Over the past ten years considerable effort has been deployed in the areas of MS-SOFCs including the development of: MS-SOFC stack [10, 18, 19], barrier layers [20-23], catalyst deposition techniques [12, 22, 24-26], protective coatings [27], and alloys for interconnects [18, 19, 28]. Stack lifetime demonstrations in anode supported cells [29] and ferritic steel substrate supported SOFCs [18] have also been demonstrated . For instance, Topsoe Fuel Cells demonstrated anode supported stack operation with coated FeCr-based interconnects that generated power for 13,000h with minimal degradation [29], and Ceres Power demonstrated operation up to 6,400h with 0.3-0.45%/khr degradation in ferritic steel substrate supported

SOFCs [18]. However, in both demonstrations the power density is substantially low, and not compatible with vehicular applications.

On the other hand, progress in MS-SOFC peak power density is rather stagnated, remaining typically between 50 and 500 mW cm^{-2} in the temperature range of 650 °C to 850 °C [11, 23, 25, 26, 30-34]. Substantially higher power is necessary for application in small passenger vehicles, in concert with tolerance to intermittent fuel flow and continuous load variation. Recently, significant improvements in stainless steel MS-SOFC performance were achieved at LBNL using symmetric-architecture MS-SOFCs and infiltrated LSM cathode and SDCN anode (peak power of 1.0 W cm^{-2} at 700 °C and 1.9 W cm^{-2} at 800 °C) [12], DTU using a single layer metal support and LSC cathode (peak power of 0.9-1.0 W cm^{-2} at 700 °C) [35], and TU Wien using LSCF cathode (peak power of 0.7 W cm^{-2} at 750 °C) [36]. In this work, we report significant further progress in cell materials, structures, and catalyst composition and processing using the cell architecture established in our previous work [1-3, 12, 28, 37]. YSZ electrolyte is replaced with higher-conductivity 10Sc1CeSZ and the electrolyte thickness is significantly reduced. Multiple cathode and anode catalysts are evaluated, and fabrication methods are optimized to further increase the cell peak power. The conventional cathode catalyst composition lanthanum strontium manganite (LSM) cathode is replaced with more active praseodymium oxide (Pr_6O_{11}) and the Ni content of the Ni and Sm-doped ceria (SDCN) anode is increased. Catalyst precursor chemistry, thickness of each cell layer, cell sintering conditions, backbone porosity, and catalyst firing temperature are optimized. Aggregating these improvements results in unprecedented performance for stainless steel MS-SOFCs.

2. Experimental methods

2.1 Cell fabrication

Green cells were assembled by laminating individual 10Sc1CeSZ (DKKK, Japan) or stainless steel (P434L alloy, water atomized, Ametek Specialty Metal Products) layers prepared by tape-casting. The layers were prepared with polymethyl methacrylate poreformer beads (Esprix Technologies) and water-based tape-casting binder. The resulting symmetric-structure metal-supported MS-SOFCs were laser-cut (Hobby model, Full Spectrum Laser) from the laminated tape-cast layers and the edges were cleaned with an air duster to remove any loose particles. Cells were then debinded by firing in air in a box furnace at 525 °C for 1h with 0.5 °C min^{-1} heating rate to slowly remove the binder and poreformer. The cells were then sintered at 1350 °C for 2h in a tubular furnace while flowing 2% hydrogen in argon. The resulting cells were 30 mm in diameter with 1 cm^2 active area, had 200 μm thick porous metal supports, 25 μm thick porous cathode and anode backbones, and 7 μm or 12 μm (two configurations) thick 10Sc1CeSZ electrolyte. More details about optimization of each cell layer can be found in our previous work [12].

2.2 Catalyst precursors and cell infiltration

Precursor mixtures of metal nitrates (Sigma Aldrich) were prepared with the intended final stoichiometric composition. A surfactant, Triton-X 100 (Sigma Aldrich) with loading of 0.3 g per 2 g of resulting catalyst was added to metal nitrates and dissolved in 20 to 100 wt% (vs. catalyst) of water. More detailed description can be found in our previous report [12]. The areas of MS-SOFCs that were not intended to be infiltrated were covered with acrylic paint mask (Liquitex). The cells were then fired at 3 °C min^{-1} heating rate to 600 °C or 850 °C for 30 min in

air to convert the precursors to the intended oxide phases [12]. The cells were re-infiltrated a number of times: (1) cathodes were infiltrated a total of three times, with firing at 850 °C, 600 °C, and 600 °C (unless composite cathodes were used); (2) while anodes were infiltrated three to four times, with firing at 850 °C, 600 °C, 600 °C, and 600 °C. XRD measurements on catalyst powders were obtained using a Bruker D2 Phaser powder diffractometer.

2.3 Cathode candidates

Five categories of cathode catalysts were screened in full cells, including: (1) perovskites: $La_{0.85}Sr_{0.15}MnO_{3-\delta}$ (LSM), $La_{0.8}Sr_{0.2}FeO_{3-\delta}$ (LSF), $LaNi_{0.6}Fe_{0.4}O_{3-\delta}$ (LNF), $(La_{0.60}Sr_{0.40})_{0.95}Co_{0.20}Fe_{0.80}O_{3-\delta}$ (LSCF), $La_{0.6}Sr_{0.4}CoO_{3-\delta}$ (LSC), $Sm_{0.5}Sr_{0.5}CoO_{3-\delta}$ (SSC); (2) nickelates: $Pr_2NiO_{4+\delta}$ (PNO), $La_2NiO_{4+\delta}$ (LNO), $Nd_2NiO_{4+\delta}$ (NNO); (3) praseodymium oxide (PrOx); (4) binary composites: $La_{0.85}Sr_{0.15}MnO_{3-\delta}-Sm_{0.20}Ce_{0.80}O_{2-\delta}$ (LSM-SDC), $Pr_6O_{11}-Sm_{0.20}Ce_{0.80}O_{2-\delta}$ (PrOx-SDC), $Sm_{0.5}Sr_{0.5}CoO_{3-\delta}-Sm_{0.20}Ce_{0.80}O_{2-\delta}$ (SSC-SDC); and (5) ternary composites: $La_{0.85}Sr_{0.15}MnO_{3-\delta}-Sm_{0.20}Ce_{0.80}O_{2-\delta}-Pr_6O_{11}$ (LSM-SDC-PrOx), and $Sm_{0.5}Sr_{0.5}CoO_{3-\delta}-Sm_{0.20}Ce_{0.80}O_{2-\delta}-Pr_6O_{11}$ (SSC-SDC- PrOx).

2.4 Cell testing

Complete cells were mounted on 410 stainless steel rigs using GM31107 glass paste (Schott, Germany). Each side of the cell was spot-welded with two NiCr wires, each carrying a small Pt mesh for good electrical contact. The applied glass paste was heated to 200 °C at 2 °C min^{-1} and then heated to 700 °C at 10 °C min^{-1} and held for one hour. The cell was then flushed with nitrogen before hydrogen humidified at room temperature was introduced to the anode. The cathode side was exposed to static air or specified air flow. The i-V and EIS measurements were recorder with a VMP3 multichannel potentiostat and current booster (Biologic).

3. Results and discussion

The symmetric-architecture MS-SOFC design comprises a thin electrolyte sandwiched between ceramic electrode backbones and stainless steel metal supports, **Fig. 1a-b.** The porous structure is designed for cathode and anode catalyst infiltration. To improve cell performance beyond that discussed in our previous reports [2, 3, 12, 37], several features of the cell configuration were systematically varied, including: electrolyte thickness, backbone thickness and porosity, electrolyte and backbone composition, and catalyst materials.
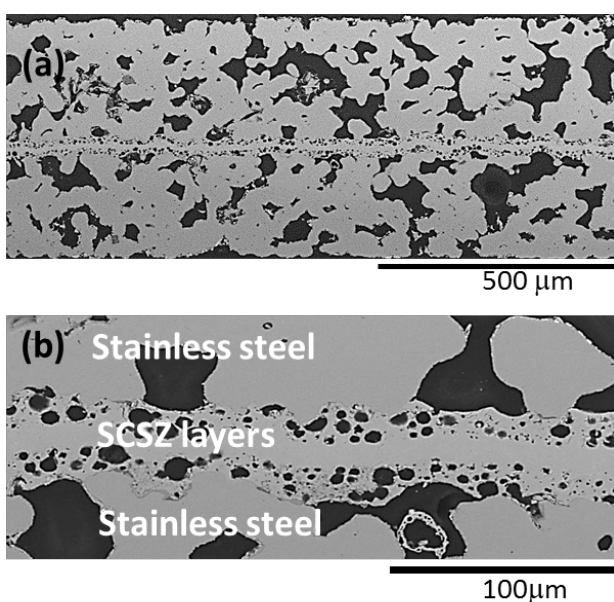

Fig 1. MS-SOFC cell structure. (a,b) Cross sectional SEM images of symmetric MS-SOFC structure.

3.1 Electrolyte and backbone composition

For successful implementation in MS-SOFCs, a candidate electrolyte must be stable under reducing atmosphere during high temperature (1350 °C) sintering and compatible with the stainless steel metal support. This is on contrast to conventional all-ceramic SOFCs where cells are typically sintered in air. We previously demonstrated successful tape casting and co-sintering

of YSZ (8 mol% yttria) electrolyte and electrode backbones with 434 stainless steel [12]. The desire to increase MS-SOFC performance, however, suggests the electrolyte conductivity must be increased [38, 39]. Cubic 10 mol% Sc_2O_3 stabilized zirconia (10ScSZ, $\sigma_{tot,10ScSZ}= 7.0$ S m^{-1} at 700 °C) has similar properties and higher conductivity when compared to YSZ ($\sigma_{tot,YSZ}= 2.5$ S cm^{-1} at 700 °C) [40], and is therefore an obvious candidate. Kazlauskas et al. [40, 41] found that the grain conductivity values for scandia-ceria-stabilized zirconia (10Sc1CeSZ, SCSZ) [40] coincided with those measured for 10ScSZ at temperatures above 550 °C. The addition of 1 mol% CeO_2 had no apparent effect on the charge transport and dielectric properties of cubic 10ScSZ, but was found to beneficially stabilize the cubic phase at lower temperatures [40]. Therefore, SCSZ was selected as the electrolyte and electrode backbone composition in this work.

Well-matched linear shrinkage of the ceramic layers and metal support is imperative for single step co-sintering of MS-SOFCs, and is the case for YSZ, **Fig. 2a**. Early shrinkage of the metal keeps the ceramic layers in compression to avoid cracking during sintering; this is especially important during incipient sintering of the ceramic layers before significant mechanical strength is achieved. The ceramic dominates the cell sintering, suggesting that any ceramic that sinters later than the metal is acceptable for MS-SOFCs. Compared to YSZ, SCSZ provides improved sintering match to stainless steel, thus fulfilling this requirement [2, 12, 28]. For both YSZ and SCSZ, full density is achieved at 1350 °C, **Fig. 2b**.

Switching from YSZ to SCSZ electrolyte decreased R_{ohm} from 0.09 Ω cm^2 to 0.06-0.065 Ω cm^2 at 700 °C, due to increased conductivity [40], **Fig. 2c**. To further reduce the ohmic resistance

(R_{ohm}) of the cell, thinner (7 μm) SCSZ electrolyte tape was fabricated, which further decreased R_{ohm} to 0.037 Ω cm^2 at 700 °C, **Fig. 2c**. This is almost a threefold decrease when compared to our previous cells [12] with YSZ electrolyte.
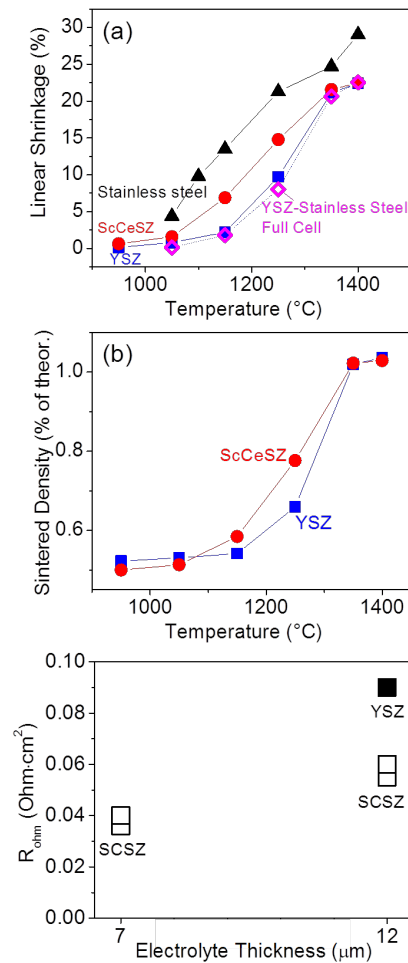

Fig 2. Comparison of YSZ and SCSZ electrolyte. (a) Linear shrinkage for individual cell components and a full cell. (b) Densification of the electrolyte. (c) Ohmic polarization in full cells as function of electrolyte composition and thickness.

3.2 Cathode selection

Catalyst screening was performed on YSZ-based MS-SOFCs with 12μm YSZ electrolyte thickness, in parallel with implementation of SCSZ electrolyte (Section 3.1). The best catalyst candidates were then implemented in SCSZ-based cells, as described in more detail in section 3.5. The cathode compositions tested in cathode/YSZ/SDCN$_{20}$ MS-SOFC cell configuration are summarized in **Table 1**. Five families of cathode catalysts were considered: (1) perovskite cathodes [42-45], (2) nickelates [46-49], (3) praseodymium oxide [50-55], (4) binary layered composites [56-58], and (5) ternary layered composites. The measured open circuit voltage (OCV) for cells with different cathode catalysts was 1.10 ± 0.02 V (theoretical is 1.12 V in 3% humidified hydrogen); the observed variations in performance arise from the cathode catalysts themselves. Small variation in OCV values for cells with different catalysts may be due to presence of small pinholes in the electrolyte since the catalyst loading and precursor concentrations are kept consistent. Representative i-V and power density curves for cells with LSM, SSC, and NNO electrodes at 700 °C are shown in **Fig. 3a**.

3.2.1 Perovskites

For perovskite cathodes, the peak power (P$_{max}$) obtained from the corresponding i-V curves at 700 °C ranged between 0.7 and 1.0 W cm^{-2}, **Table 1**. SSC and LSC exhibited the highest peak power while LSM, LSF, LNF, and LSCF showed similar performance of ~0.8 W cm^{-2}. The ohmic (R$_{ohm}$) and electrode (R$_{pol}$) polarization, obtained from the corresponding EIS spectra measured at OCV, is also presented in **Table 1** and **Fig. 3b**. The total cell resistance (R$_{tot}$) is dominated by the R$_{pol}$ (ranging from 0.2 Ω cm^2 for SSC to 0.35 Ω cm^2 for LSM), and the variation in R$_{ohm}$ (inductance corrected values) between different catalysts are smaller in

magnitude (ranging from 0.07 to 0.15 Ω cm^2), **Fig. 3c**. SSC, LSC, and LSM provide the lowest

R_{ohm}, which may be attributed to higher ionic and/or electronic conduction but may also indicate

better infiltrate distribution in the electrode. The electronic conductivity for the conducting

ceramics at 700 °C (e.g. $\sigma_{e,SSC}$ = 1500 S cm^{-1} [59], $\sigma_{e,LSC}$ = 1360 S cm^{-1} [60, 61], $\sigma_{e,LSM}$ = 180 S

cm^{-1} [45, 60], $\sigma_{e,LSCF}$ = 190 S cm^{-1} [62, 63]) supports these results. R_{tot}, however, is influenced by

multiple parameters including: crystal phase, particle size distribution, and extent of sintering of

the catalyst. It is likely that each catalyst requires tailored optimization, and the fabrication

conditions used for screening may not be optimum for some of the catalysts.

Table 1. Summarized full cell parameters with various cathode catalyst compositions at 700 °C.

Abbreviation	OCV (V)	Peak Power (W cm^{-2})	R_{ohm} at OCV (Ω cm^2)	R_{pol} at OCV (Ω cm^2)	R_{tot}* at OCV (Ω cm^2)	ASR$^+$ at 0.7 V (Ω cm^2)
Perovskites						
LSM	1.12	0.9	0.09	0.36	0.45	0.26
LSF	1.09	0.7	0.14	0.33	0.47	0.32
LNF	1.11	0.7	0.13	0.25	0.38	0.31
LSCF	1.10	0.8	0.15	0.30	0.45	0.25
LSC	1.09	1.0	0.08	0.22	0.30	0.23
SSC	1.10	1.0	0.07	0.2	0.27	0.23
Nickelates and PrOx						
PNO	1.09	0.6	0.09	0.52	0.61	0.32
LNO	1.10	1.0	0.12	0.16	0.28	0.23
NNO	1.11	1.0	0.09	0.18	0.27	0.24
PrOx	1.12	1.3	0.08	0.18	0.26	0.14
Binary and Ternary Composites						
LSM-SDC$_{600}$	1.09	1.1	0.09	0.19	0.28	0.19
LSM-SDC$_{850}$	1.12	1.1	0.09	0.21	0.30	0.18
PrOx-SDC	1.10	1.2	0.08	0.20	0.28	0.17
SSC-SDC	1.11	1.1	0.08	0.22	0.30	0.18
LSM-SDC-PrOx	1.12	1.1	0.08	0.21	0.29	0.19
SSC-SDC-PrOx	1.09	1.1	0.09	0.23	0.32	0.20

* R_{tot} was obtained from the corresponding EIS spectra.

$^+$ ASR was obtained from the derivative of the i-V curve at specific current density corresponding to 0.7 V.
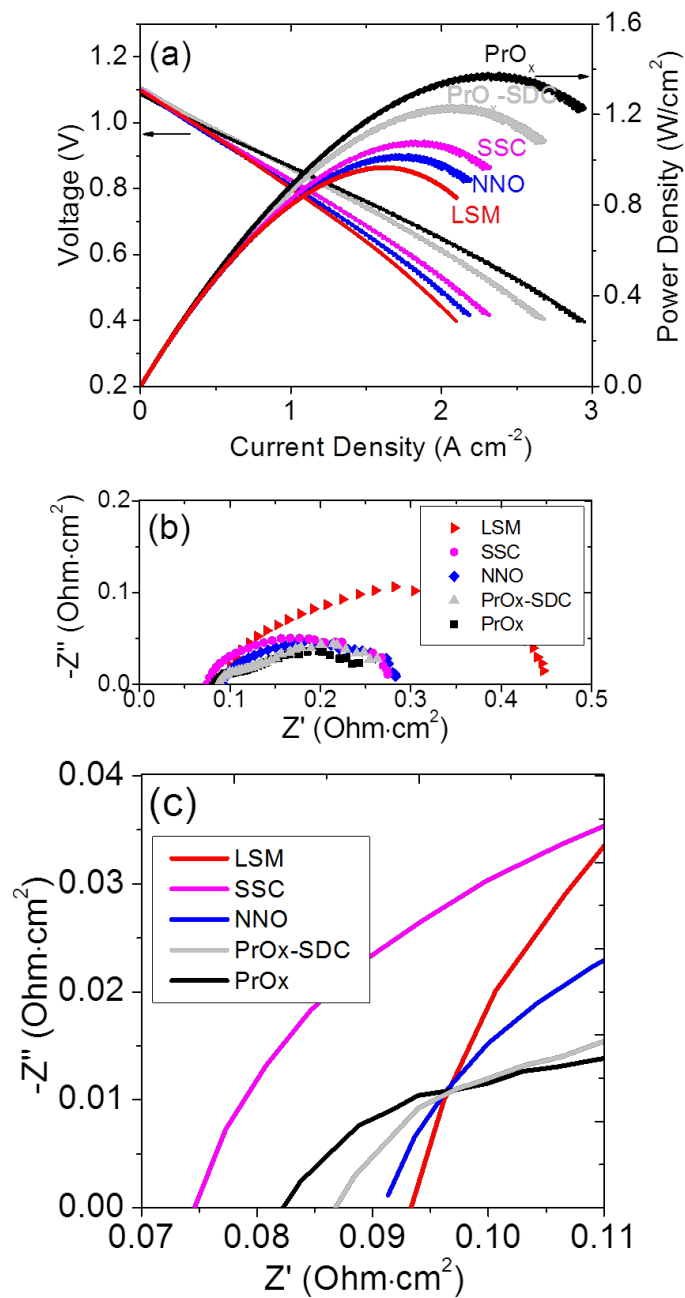
Fig 3. Impact of cathode composition. Full-cell performance with various cathode catalysts, YSZ electrolyte, and SDCN20 anode at 700°C. (a) i-V and power density curves for selected perovskites, nickelates, PrOx, and composite electrodes in full cells. (b) Corresponding EIS spectra at OCV and 700 °C. (c) Corresponding R_{ohm} for full cells with various cathode catalysts at 700 °C and OCV.

3.2.2 Nickelates

The cells with nickelate cathodes show similar performance to the perovskites, **Table 1**. LNO and NNO show a peak power of 1.0 W/cm^2 (**Fig. 3a**), while PNO shows lower performance of 0.6 W/cm^2. These findings are inconsistent with the literature; due to higher catalytic activity for ORR, PNO is expected to have higher performance than LNO and NNO ($E_{a,PNO}$ = 0.87 eV vs. $E_{a,LNO}$=1.3 eV vs. $E_{a,NNO}$=1.15 eV) [50]. The purity of the nickelate phase in ceramic electrodes can be closely correlated to the cell performance (the higher the phase purity the higher the performance) [48-51]. We surmise the sintering temperature is too low for PNO, but to avoid oxidation, it is limited to <900 °C. Therefore, it is possible that the nickelate sintering temperature (mainly PNO) is too low for single phase formation [50, 53]. Large R_{pol} for PNO, while R_{ohm} is similar to LNO and NNO, indicates that the bulk of the electrode is limiting the cell performance [48, 50, 51]. These results underscore the importance of screening the catalysts using processing conditions that are relevant to MS-SOFCs.

3.2.3 Pr$_6$O$_{11}$

Pr$_6$O$_{11}$ (PrOx) is known to be a stable [48] phase transformation byproduct of PNO under cell operating conditions in the temperature region between 600 and 850 °C [50, 51]. Recent efforts have elucidated the effect of PrOx on cell performance. Nicollet et al. [55] demonstrated that PrOx infiltration into a porous Gd-doped ceria cathode backbone leads to substantial peak power improvements, from 0.40 W cm^{-2} to 0.80 W cm^{-2} at 600 °C. Dogdibegovic et al. [52-54] also showed that a thin film of PrOx on top of the Gd-doped ceria buffer layer between the electrolyte and cathode increased the cell performance by 30% at 0.80V in the temperature range between 650-850 °C. The mechanism was shown to be extension of the mixed conduction region for

ORR arising from Pr-doping into the Gd-doped ceria buffer layer [54]. Although the total conductivity of PrOx (σ_{tot}= 2.3 S cm^{-1} at 700 °C) [55] is significantly lower when compared to PNO (σ_{tot}= 84 S cm^{-1} at 700 °C) [50] and perovskite ceramics (see section 3.2.1), the oxygen ion transport properties seem to be enhanced. In particular, the oxygen diffusion (D) and surface exchange (k) coefficients for PrOx (600 °C: D=3.4·10^{-8} cm^2 s^{-1} and k=5.4·10^{-7} cm s^{-1}) [55] are higher than for PNO (600 °C: D=2·10^{-8} cm^2 s^{-1} and k=5·10^{-7} cm s^{-1}) [64], LSCF (600 °C: D=4.0·10^{-10} cm^2 s^{-1} and k=2.0·10^{-8} cm s^{-1}) [64], and LSM ceramics (700 °C: D=2·10^{-16} cm^2 s^{-1} and k=1·10^{-9} cm s^{-1}) [65]. It is imperative to note, however, that studies of transport properties were performed on dense ceramic pellets sintered well above 1000 °C, while the activity of nano-scale PrOx catalyst in MS-SOFCs remains to be investigated.

Of all cathode catalysts tested in this work, PrOx yields the highest peak power (P_{max}=1.34 W/cm^2), **Fig. 3a** and **Table 1**. Although the R_{ohm}=0.075 Ω cm^2 and R_{pol}=0.185 Ω cm^2 (at OCV) values are similar to those found for LSC, SSC, LNO and PNO under OCV (**Fig. 3b**), the cell ASR under operating conditions is lower (**Table 1**) providing the highest peak power. With increase in current density the cell with PrOx catalyst shows the lowest i-V slope, indicating good ORR catalysis under cell operating conditions.

3.2.4 Binary and ternary layered composites

In conventional composite electrodes the entire electrode bulk acts as a composite material (pre-mixed ionic and electronic conductors), which leads to increase in the cell performance [52-54, 56-58]. For instance, mixing of an ionic conductor (e.g SDC) with an electronic conductor (LSM) provides a shorter pathway for ionic transport within the electrode. Furthermore, the

thickness of the electrode contributing to ORR can be effectively increased, allowing more active surface area for catalysis [52]. As a result, electrode R_{pol} is typically reduced, as previously demonstrated in a number of literature reports on conventional composites including: LSM-SDC and LSM-YSZ [56, 57], LSCF-SDC [57, 58, 66], and PNO-GDC composites [58].

Here, we implement the infiltration method to generate layered composites inside the porous ceramic backbones. Dual- and triple-layered composite infiltrates have been developed. Contrary to conventional composites, binary and ternary layered composite electrodes in this work consist of two or three different catalysts infiltrated layer by layer, with each layer carrying a specific functionality to improve the overall electronic and ionic conductivity of the electrode. For instance, in the case of LSM-SDC-PrOx (**Table 1**) the LSM provides good ionic and electronic conduction at the triple phase boundary (TPB), SDC provides good ionic conduction, and PrOx acts as a bulk catalyst for the oxygen reduction reaction (ORR).

LSM-SDC composites (with SDC fired at 850 °C) provide 38% increase in peak power when compared to LSM, **Fig, 3a**. Ternary composites (**Table 1**) including LSM-SDC-PrOx and SSC-SDC-PrOx show similar performance to LSM-SDC (P_{max} of 1.1 W cm^{-2}). The cells with PrOx catalyst infiltrated as the first layer (ex. PrOx and PrOx-SDC) exhibit the highest peak power (P_{max} of 1.3 W cm^{-2} and 1.2 W cm^{-2}, respectively), **Fig. 3a**. This may indicate that PrOx layer at the TPB is the most effective mixed conductor. It has been previously reported that Pr-doped SDC or GDC extends the mixed conducting region of the electrode [53, 54] and leads to substantial performance improvements in the full cell [54]. Hence, it is possible that elemental Pr diffuses at a narrow PrOx/SCSZ interface during catalyst firing and operation, making the

PrOx/SCSZ interface more electronically conductive, consistent with the low R_{ohm} values, **Fig. 3b**.

3.3 Anode selection

Anode catalyst selection was conducted on the LSM/YSZ/anode MS-SOFC cell configuration. Infiltrated Ni is known to coarsen quickly during operation [7], and addition of SDC can stabilize the Ni particles and reduce the degradation rate [8, 67]. In this work, the Ni concentration mixed with SDC ranged from 0-50 vol.% in an attempt to further increase the electronic conduction in the anode. Increased Ni content leads to an overall decrease in R_{pol} (14% decrease from SDC_{90}-Ni_{10} to SDC_{50}-Ni_{50}) and R_{omh} (21 % decrease), **Fig. 4a**. Surprisingly, Ni-free SDC also showed some initial activity for hydrogen oxidation (R_{pol}=0.61 Ω cm^2). This may be due to possible chromium oxide or iron oxide diffusion from the metal support into SDC during the catalyst firing process in air, allowing for some catalysis at the backbone/SDC/metal interface. Similar R_{ohm} value to cells with Ni-containing SDC may indicate that ohmic resistance is dominated by the electrolyte and the backbones (65 μm total), suggesting that Ni percolation was not achieved. A practical Ni content balance was found based on R_{ohm} and R_{pol} values; the SDCN40 composition was selected for high performance MS-SOFCs.

Ju et al. [68] demonstrated that co-doping of ceria with Mn and Fe leads to increased electronic conductivity and surface activity toward the electrochemical oxidation of hydrogen. Here, in order to mitigate the lack of Ni percolation while maintaining sufficient electronic conduction, SDC was replaced with $Ce_{0.6}Mn_{0.3}Fe_{0.1}O_{2-\delta}$ (CMF) for the Ni-free and $Ce_{0.6}Mn_{0.3}Fe_{0.1}O_{2-\delta}$/20 vol.% Ni (CMFN) anode compositions, **Fig. 4a**. Although this strategy was not successful in

significantly improving ohmic impedance, it is interesting to note that the Ni-free CMF provides similar performance to SDCN compositions. We anticipate this would be advantageous for avoiding coking when using carbon-containing fuels.
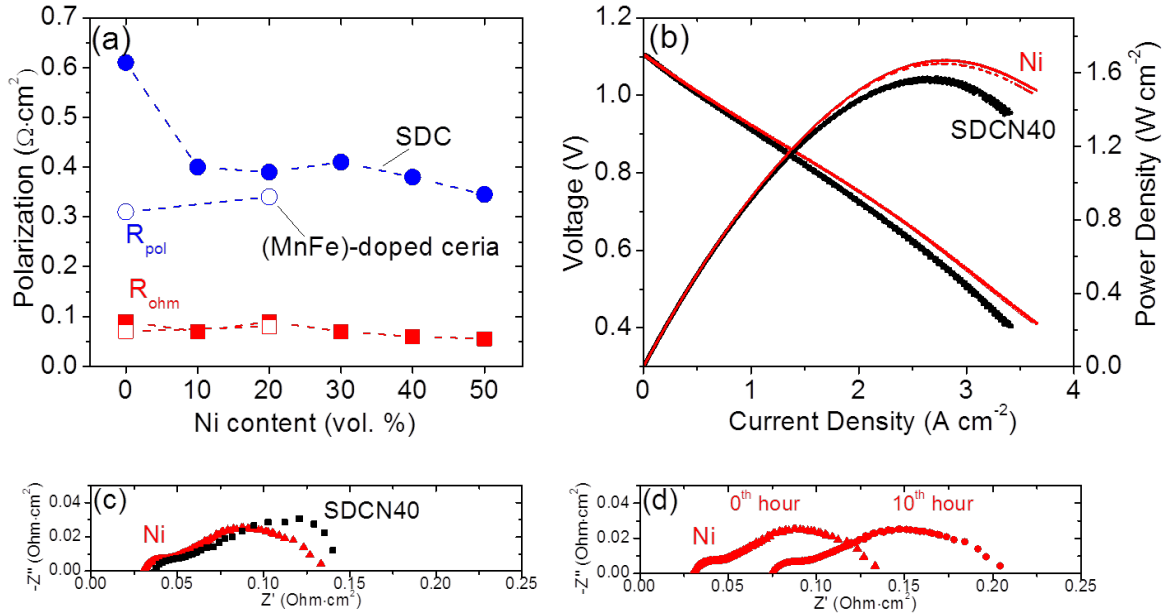

Fig. 4. Impact of anode composition. (a) Measured ohmic (solid red square) and electrode (solid blue circle) polarization for LSM/YSZ/anode cell configurations with varying Ni concertation in Ni-containing SDC at 700 °C and OCV. The ohmic (open red square) and electrode (open blue circle) polarization for Mn,Fe co-doped ceria is also illustrated. (b) i-V and power density curves for two cells with SDCN40 anode (black lines) and two cells with Ni anode (red lines) at 700 °C in PrOx/SCSZ/anode cell configuration. (c) Corresponding EIS spectra at OCV and 700 °C for the cells with SDCN40 and Ni anodes described in (b); (d) A ten hour stability of the cell with Ni anode during 700 °C hold at OCV.

In an attempt to further enhance the electronic conduction in the anode by achieving a metallic percolating electronic path to the anode/electrolyte interface, an anode with pure Ni infiltrated was also tested. In this particular case SDC was not present and Ni content was 100 vol. % of the

18

anode catalyst. The peak power density of 1.62 W W cm^{-2} at 700 °C was measured with two reproducible cells, **Fig 4b**. Minimal improvement in R$_{ohm}$ and R$_{pol}$ indicate that further performance improvements of MS-SOFCs are not currently limited by the electronic conduction of anode, **Fig 4c**. Furthermore, in the absence of SDC, rapid Ni coarsening after only 10 hours leads to performance degradation, **Fig. 4d**; this degradation mode has been studied in detail previously [7].

3.4 Further MS-SOFC optimization

The MS-SOFC sintering temperature was optimized in the range 1250 to 1400 °C. A practical balance between densification of the electrolyte, porosity of the ceramic backbones and metal supports is required to provide large enough pores for catalyst infiltration and mass transport. Single step co-sintering of the green tapes in 2%H$_2$/Ar at 1350 °C for 2 hours provided the optimum cell microstructure and the highest cell performance, **Table 2**. The catalyst firing temperature was also optimized in the range of 600 - 850 °C, the maximum chosen to prevent oxidation of the metal support. Multiple infiltrations provide the opportunity to fire the same catalyst composition at different temperatures. Firing the first layer of infiltrated LSM at 850°C to improve conduction, and subsequent layers at 600°C to maintain high surface area was previously found to be an effective strategy [12]. The catalyst sintering ratio (850 °C/600 °C) for PrOx/YSZ/SDCN40 cells was investigated here. Sintering the first catalyst layer at 850 °C (good contact at the triple phase boundary), followed by sintering at 600 °C (large catalytic area) provides the highest cell performance along with the electrode thickness of 25 μm, **Table 2**.

XRD of PrOx catalyst fired at both 600 °C and 850 °C in air showed a single monoclinic Pr_6O_{11} phase, with the peak intensities retaining the same ratio at both firing temperatures, indicating homogeneous bulk PrOx, **Fig. 5a**. In contrast, LSM catalyst shows partial phase purity at both temperatures and temperature increase leads to more pronounced signature reflections, **Fig. 5b.**

Table 2. Impact of fabrication parameters on peak power and R_{tot} (at OCV) at 700 °C.

	Peak power (W cm^{-2})	R_{tot} (Ω cm^2)
Cell Sintering Temperature (°C)		
1250	0.65	0.5
1300	0.8	0.4
1350	1.3	0.25
1400	0.9	0.37
Number of 850 °C/600 °C catalyst sintering steps		
0/3	1.1	0.29
1/2	1.3	0.24
2/1	0.9	0.35
3/0	0.7	0.42
Electrode thickness (μm)		
12	0.8	0.47
18	0.9	0.46
25	1.3	0.26
30	0.9	0.43
50	0.8	0.38

These results indicate that MS-SOFC catalyst sintering temperatures are well suited for the PrOx catalyst, but higher temperature may be required to obtain a single LSM phase. SDCN40 anode catalyst was fired in air at 600 °C and 850 °C and then reduced in 3% humidified hydrogen at 700 °C. XRD patterns show mainly SDC phase and the major nickel oxide (air) or Ni (reduced) signature peaks, indicating the expected SDCN40 phase is achieved, **Fig. 5c**. The intended Pr_6O_{11} and SDCN$_{40}$ stoichiometric compositions of the nanocatalysts are in good correlation with the actual composition in the MS-SOFCs. It is imperative to note that nanocatalysts are used in

MS-SOFCs, so the catalytic behavior may be different from the usual micron-scale particles in all-ceramic SOFCs. The catalyst morphology, porosity, sintering, and mass loading could all impact the cell performance, and phase purity is not a requirement for functionality.
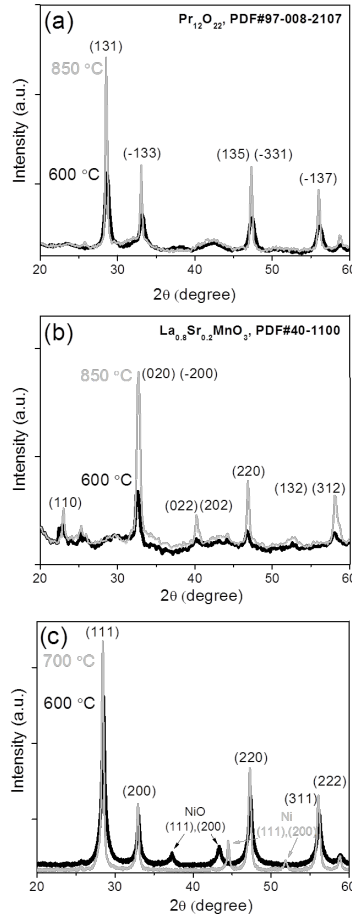

Fig 5. Catalyst phase purity. (a,b) Powder X-ray diffraction on PrOx and LSM cathode catalysts sintered at 600 °C (black) and 850 °C (gray) for 30min. (c) X-ray diffraction patterns for SDCN40 anode catalyst after firing in air at 600 °C for 30 min (black) and upon reduction in 3% humidified hydrogen at 700 °C for 1 hour (gray).

3.5 High performance MS-SOFCs

Aggregating the improvements identified in Sections 3.1-3.4, including PrOx cathode catalyst composition, SDCN40 anode ratio, thin SCSZ electrolyte (7 μm), and optimized fabrication procedures, resulted in unprecedented performance for MS-SOFCs with stainless steel metal support. Peak power of 1.56 W cm^{-2} at 700 °C, and 2.85 W cm^{-2} at 800 °C (extrapolated) was obtained, **Fig. 6a**. The i-V polarization is approximately linear, with concentration polarization occurring only at high current density. The corresponding EIS spectra, obtained at OCV, illustrate decrease in R_{ohm} by twofold, and decrease in R_{pol} by 25% when increasing the temperature from 700 °C to 800 °C, **Fig. 6b**. The R_{tot} decreases with increase in operating temperature due to (1) increase in ionic mobility through the electrolyte and at the TPB, (2) lowered activation barrier for ORR, and (3) enhanced MIEC properties of the catalyst [48].
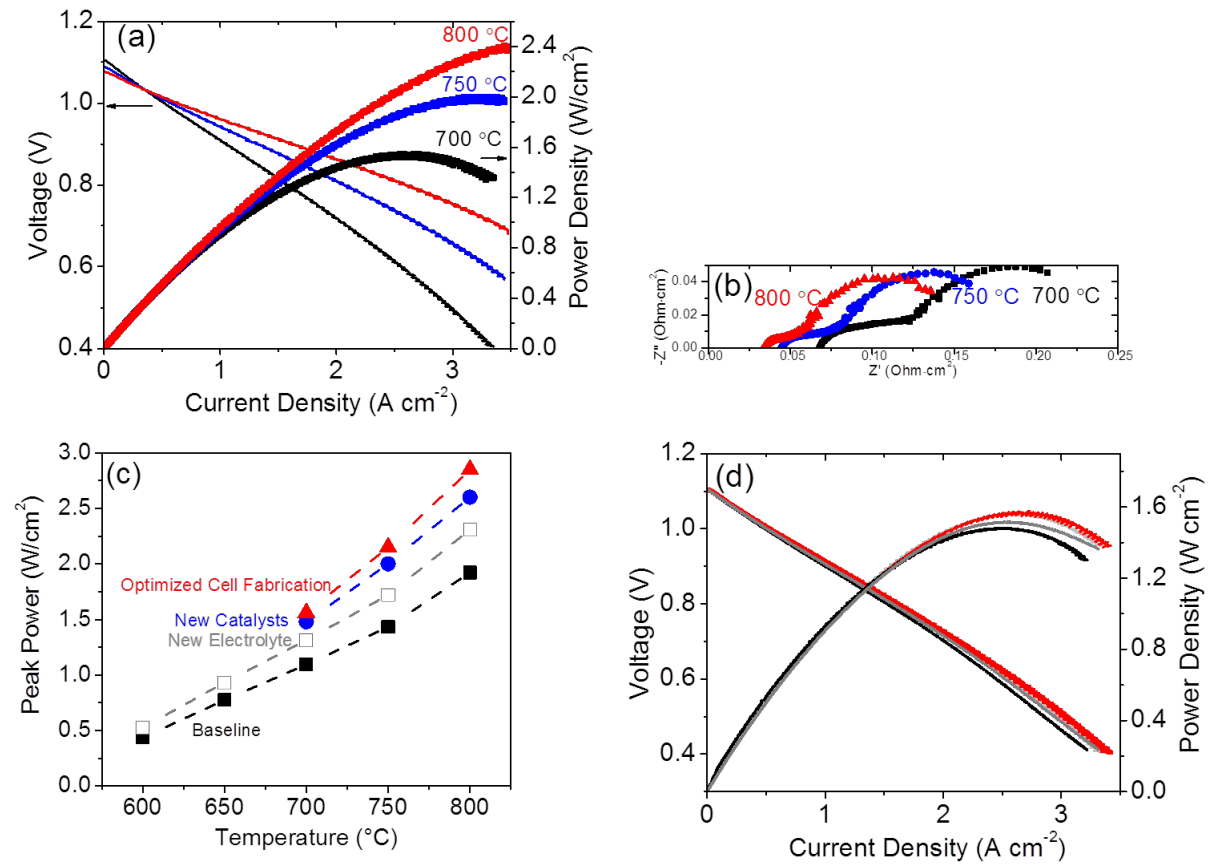
Fig. 6. Performance of improved cell. (a) i-V and power density curves for PrOx/SCSZ/SDCN40 cell configuration and improved cell fabrication. (b) The corresponding EIS plots under the same temperature range at OCV. (c) Progress in peak power with various cell improvements. (d) Performance reproducibility at 700 °C.

Contributions to the overall improvement of MS-SOFC performance in this work were separately quantified. For the LSM-based cells, switching from YSZ to SCSZ electrolyte led to increase in peak power from 1.1 to 1.3 W cm^{-2} at 700 °C. A Further catalyst development (PrOx cathode and SDCN40 anode) lead to increase in peak power to 1.5 W cm^{-2}, while the optimized fabrication procedure with the new catalysts leads to peak power of 1.56 W cm^{-2} at 700 °C, **Fig. 6c**. The overall peak power at 750 °C was increased from 1.43 W cm^{-2} to 2.0 W cm^{-2}, and from 1.9 W/cm^2 to 2.85 W cm^{-2} (extrapolated) at 800 °C.
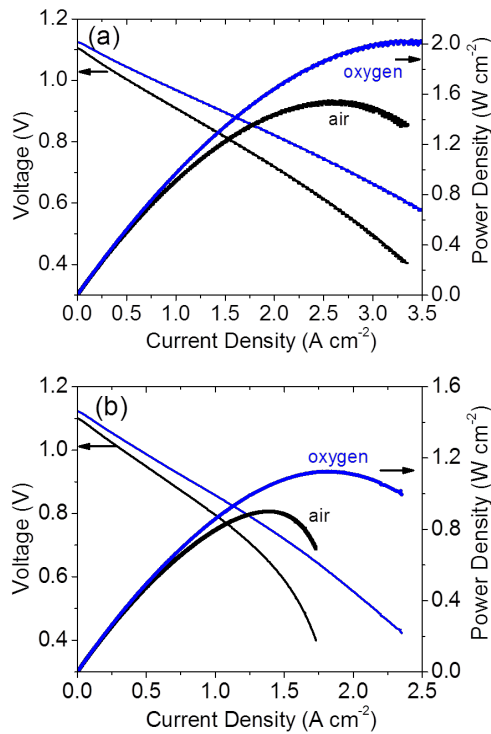
Fig. 7. Performance in different oxidants. The i-V and power density curves at 700 °C in air (black) and oxygen (blue) for cathode/SCSZ/SDCN40 cell configuration with (a) PrOx cathode and (b) LSM-SDC cathode.

Multiple cells were fabricated to assess cell-to-cell variation and demonstrate reproducibility. All cells achieved OCV of 1.10 ± 0.02 V, which indicates dense electrolyte, absence of pinholes, and good sealing. Peak power ranged from 1.44 to 1.56 W cm^{-2}, **Fig. 6**d. Reasonable variation in P$_{max}$ (<8%) indicates consistent cell fabrication. Cells were operated with both flowing air and oxygen (300 sccm) to investigate the cathode mass transport limitation. Power density improvement of approximately 30% was observed for both cathode compositions (PrOx and LSM) when switching from air to oxygen, primarily as a result of higher OCV and reduced concentration polarization, **Fig. 7a-b**. The PrOx/SCSZ-7µm/SDCN40 cell with cathode exposed to oxygen shows peak power of 2.0 W cm^{-2} at 700 °C. Similar performance improvement is anticipated for pressurized systems.

4. Conclusions

Symmetric-architecture MS-SOFCs have been optimized for high performance, motivated by the requirements for use in vehicle range extenders. Development of the new electrolyte and backbone ceramics, along with selection of cathode and anode catalysts led to approximately 50% increase in power density compared to our previous work [2]. Higher conductivity SCSZ electrolyte and backbones were used instead of YSZ, and conventional LSM cathode and SDC-Ni anode were replaced with Pr_6O_{11} cathode and higher Ni content in anode. The power density of 1.56 W cm^{-2} at 700 °C in air and 2.0 W cm^{-2} in oxygen (with the cell R$_{tot}$ of 0.14 Ω cm^2 at

OCV) is the highest cell performance reported for stainless steel metal supported MS-SOFCs to date. Multiple cells showed reproducible performance.

Cell ASR is shown to be dominated mainly by the cathode polarization and cell configuration. Performance is very sensitive to cathode composition, but relatively insensitive to the Ni content in SDCN anode. The cell fabrication procedure (sintering temperature, catalyst firing temperature) significantly impacts the cell performance. Optimization of individual cell layers (electrolyte and backbone composition, thickness, and porosity) also yielded substantial improvements in the MS-SOFC power density.

or assumes any legal liability or responsibility for the accuracy, completeness, or usefulness of any information, apparatus, product, or process disclosed, or represents that its use would not infringe privately owned rights.

References

[1] M. C. Tucker, G. Y. Lau, C. P. Jacobson, L. C. DeJonghe, S. J. Visco, ECS Transactions, 7 (2007) 279-284.
[2] M.C. Tucker, Journal of Power Sources, 195 (2010) 4570-4582.
[3] M.C. Tucker, G.Y. Lau, C.P. Jacobson, L.C. DeJonghe, S.J. Visco, Journal of Power Sources, 171 (2007) 477-482.
[4] Y.B. Matus, L.C. De Jonghe, C.P. Jacobson, S.J. Visco, Solid State Ionics, 176 (2005) 443-449.
[5] M.C. Tucker, International Journal of Hydrogen Energy, 43 (2018) 8991-8998.
[6] M.C. Tucker, Journal of Power Sources, 395 (2018) 314-317.
[7] M.C. Tucker, G.Y. Lau, C.P. Jacobson, L.C. DeJonghe, S.J. Visco, Journal of Power Sources, 175 (2008) 447-451.
[8] P. Blennow, J. Hjelm, T. Klemenso, S. Ramousse, A. Kromp, A. Leonide, A. Weber, Journal of Power Sources, 196 (2011) 7117-7125.
[9] J.N. T. Klemenso, P. Blennow, A. G. Persson, T. Stegk, P. Hjalmarsson, B. H. Cristense, S. Sonderby, J. Hjelm, and S. Ramousse, ECS Transactions, 35 (2011) 369-378.
[10] S.P. N. Christiansen, M. Wandel, S. Ramousse, and A. Hagen, ECS Transactions, 57 (2013) 43-52.
[11] V.V. Krishnan, Wiley Interdisciplinary Reviews-Energy and Environment, 6 (2017).
[12] M.C. Tucker, Energy Technology, 5 (2017) 2175-2181.
[13] I. Villarreal, C. Jacobson, A. Leming, Y. Matus, S. Visco, L. De Jonghe, Electrochemical and Solid State Letters, 6 (2003) A178-A179.
[14] G.Y. Lau, M.C. Tucker, C.P. Jacobson, S.J. Visco, S.H. Gleixner, L.C. DeJonghe, Journal of Power Sources, 195 (2010) 7540-7547.
[15] M.C. Tucker, H. Kurokawa, C.P. Jacobson, L.C. De Jonghe, S.J. Visco, Journal of Power Sources, 160 (2006) 130-138.
[16] R. Wang, M. Würth, U.B. Pal, S. Gopalan, S.N. Basu, Journal of Power Sources, 360 (2017) 87-97.
[17] R.F. Wang, U.B. Pal, S. Gopalan, S.N. Basu, Journal of the Electrochemical Society, 164 (2017) F740-F747.
[18] A.B. R. Leah, M. Lankin, A. Selcuk, M. Rahman, A. Clare, L. Rees, S. Phillip, S., M.a.M. Selby, ECS Transactions, 68 (2015) 95-107.
[19] P.S. A. Ansar, J. Arnold, Z. Ilhan, D. Soysal, R. Costa, A. Zagst, M. Gindrat, and T. Franco, ECS Transactions, 35 (2011) 147-155.
[20] A.A. Solouyev, S.V. Rabotkin, A.V. Shipilova, A.I. Kirdyashkin, I.V. Ionov, A.N. Kovalchuk, A.S. Maznoy, V.D. Kitler, A.O. Borduleva, International Journal of Hydrogen Energy, 40 (2015) 14077-14084.
[21] R. Nedelec, R. Neagu, S. Uhlenbruck, R. Maric, D. Sebold, H.P. Buchkremer, D. Stover, Surface & Coatings Technology, 205 (2011) 3999-4004.
[22] E.S.C. Fan, J. Kuhn, O. Kesler, Journal of Power Sources, 316 (2016) 72-84.
[23] Y. Yoo, Y.L. Wang, X.H. Deng, D. Singh, J.G. Legoux, Journal of Power Sources, 215 (2012) 307-311.
[24] R.I. Tomov, M. Krauz, A. Tluczek, R. Kluczowski, V.V. Krishnan, K. Balasubramanian, R.V. Kumar, B.A. Glowacki, Materials for Renewable and Sustainable Energy, 4 (2015) 14.
[25] C. Metcalfe, J. Kuhn, O. Kesler, Journal of Power Sources, 243 (2013) 172-180.
[26] C.S. Hwang, C.H. Tsai, J.F. Yu, C.L. Chang, J.M. Lin, Y.H. Shiu, S.W. Cheng, Journal of Power Sources, 196 (2011) 1932-1939.

[27] R. Wang, Z. Sun, U.B. Pal, S. Gopalan, S.N. Basu, Journal of Power Sources, 376 (2018) 100-110.

[28] M.C. Tucker, B. Carreon, J. Charyasatit, K. Langston, C. Taylor, J. Manjarrez, N. Burton, M. LaBarbera, and C.P. Jacobson, ECS Transactions, 57 (2013) 503-509.

[29] J.B.H. N. Christiansen, H. Holm-Larsen, S. Linderoth, P. H. Larsen, P. V., a.A.H. Hendriksen, in: Energy solutions for sustainable development. Proceedings, Risø National Laboratory, Roskilde, Denmark, 2007, pp. 357-362.

[30] Z.Y. Han, Z.B. Yang, M.F. Han, International Journal of Hydrogen Energy, 41 (2016) 10935-10941.

[31] A.M. Dayaghi, K.J. Kim, S. Kim, J. Park, S.J. Kim, B.H. Park, G.M. Choi, Journal of Power Sources, 324 (2016) 288-293.

[32] H.J. Cho, Y.M. Park, G.M. Choi, Solid State Ionics, 192 (2011) 519-522.

[33] H.J. Cho, K.J. Kim, Y.M. Park, G.M. Choi, International Journal of Hydrogen Energy, 41 (2016) 9577-9584.

[34] Y.C. Zhou, Z.C. Zhang, C. Yuan, J.L. Li, C.R. Xia, Z.L. Zhan, S.R. Wang, International Journal of Hydrogen Energy, 38 (2013) 16579-16583.

[35] J. Nielsen, Å. H.Persson, T. T. Muhl, adnd K. Brodersen, Journal of The Electrochemical Society, 165 (2018) F90-F96.

[36] D. Udomsilp, D. Roehrens, N.H. Menzler, C. Bischof, L.G.J. de Haart, A.K. Opitz, O. Guillon, M. Bram, Journal of the Electrochemical Society, 164 (2017) F1375-F1384.

[37] M.C. Tucker, L. Cheng, L.C. DeJonghe, Journal of Power Sources, 196 (2011) 8313-8322.

[38] B.E. McNealy, J. Jiang, J.L. Hertz, Journal of the Electrochemical Society, 162 (2015) F537-F546.

[39] O.H. Kwon, G.M. Choi, Solid State Ionics, 177 (2006) 3057-3062.

[40] S. Kazlauskas, E. Kazakevicius, A. Kezionis, Solid State Ionics, 310 (2017) 143-147.

[41] S. Kazlauskas, A. Kezionis, T. Salkus, A.F. Orliukas, Lithuanian Journal of Physics, 52 (2012) 231-237.

[42] S.B. Adler, Chemical Reviews, 104 (2004) 4791-4843.

[43] Y.B. Chen, W. Zhou, D. Ding, M.L. Liu, F. Ciucci, M. Tade, Z.P. Shao, Advanced Energy Materials, 5 (2015).

[44] C.W. Sun, R. Hui, J. Roller, Journal of Solid State Electrochemistry, 14 (2010) 1125-1144.

[45] A. Jun, J. Kim, J. Shin, G. Kim, Chemelectrochem, 3 (2016) 511-530.

[46] S.N. Ruddlesden, P. Popper, Acta Crystallographica, 10 (1957) 538-540.

[47] S.N. Ruddlesden, P. Popper, Acta Crystallographica, 11 (1958) 54-55.

[48] E. Dogdibegovic, W.B. Guan, J.B. Yan, M.J. Cheng, X.D. Zhou, Journal of the Electrochemical Society, 163 (2016) F1344-F1349.

[49] E. Dogdibegovic, J.B. Yan, Q.S. Cai, H.Y. Jung, Z.L. Xing, Z.E. Liu, R.W. Goettler, X.D. Zhou, Journal of the Electrochemical Society, 164 (2017) F3131-F3139.

[50] E. Dogdibegovic, Q.S. Cai, N.S. Alabri, W.B. Guan, X.D. Zhou, Journal of the Electrochemical Society, 164 (2017) F99-F106.

[51] E. Dogdibegovic, C.J. Wright, X.D. Zhou, Journal of the American Ceramic Society, 99 (2016) 2737-2741.

[52] E. Dogdibegovic, in, University of South Carolina, The institutional repository of the University of South Carolina, 2017, pp. 197-211.

[53] E. Dogdibegovic, N.S. Alabri, C.J. Wright, J.S. Hardy, C.A. Coyle, S.A. Horlick, W.B. Guan, J.W. Stevenson, X.D. Zhou, Journal of the Electrochemical Society, 164 (2017) F1115-F1121.

[54] N.S.A. Emir Dogdibegovic, Kevin Tenny,Christopher J. Wright, John S. Hardy, Christopher A. Coyle, Samuel A. Horlick, Wanbing Guana, Jeffry W. Stevenson, and Xiao-Dong Zhou, ECS Transactions, 78 (2017) 983-992.

[55] C. Nicollet, A. Flura, V. Vibhu, A. Rougier, J.M. Bassat, J.C. Grenier, International Journal of Hydrogen Energy, 41 (2016) 15538-15544.

[56] M.J. Jorgensen, M. Mogensen, Journal of the Electrochemical Society, 148 (2001) A433-A442.

[57] X.D. Zhou, J.W. Templeton, Z. Nie, H. Chen, J.W. Stevenson, L.R. Pederson, Electrochimica Acta, 71 (2012) 44-49.

[58] B. Philippeau, F. Mauvy, C. Nicollet, S. Fourcade, J.C. Grenier, Journal of Solid State Electrochemistry, 19 (2015) 871-882.

[59] S. Yang, T.M. He, Q. He, Journal of Alloys and Compounds, 450 (2008) 400-404.

[60] F. Tietz, I.A. Raj, M. Zahid, D. Stover, Solid State Ionics, 177 (2006) 1753-1756.

[61] L.W. Tai, M.M. Nasrallah, H.U. Anderson, D.M. Sparlin, S.R. Sehlin, Solid State Ionics, 76 (1995) 273-283.

[62] A. Jun, S. Yoo, O.-h. Gwon, J. Shin, G. Kim, Electrochimica Acta, 89 (2013) 372-376.

[63] G. Corbel, S. Mestiri, P. Lacorre, Solid State Sciences, 7 (2005) 1216-1224.

[64] E. Boehm, J.M. Bassat, P. Dordor, F. Mauvy, J.C. Grenier, P. Stevens, Solid State Ionics, 176 (2005) 2717-2725.

[65] E.N. Armstrong, K.L. Duncan, E.D. Wachsman, Physical Chemistry Chemical Physics, 15 (2013) 2298-2308.

[66] J.B. Yan, H. Chen, E. Dogdibegovic, J.W. Stevenson, M.J. Cheng, X.D. Zhou, Journal of Power Sources, 252 (2014) 79-84.

[67] P. Blennow, J. Hjelm, T. Klemensø, S. Ramousse, A. Kromp, A. Leonide, A. Weber, 196 (2011) 7117–7125.

[68] Y.-W. Ju, S. Ida, T. Ishihara, RSC Advances, 3 (2013) 10508-10515.